16TH EUROPEAN CONFERENCE ON EARTHQUAKE ENGINEERING THESSALONIKI 18 - 21 JUNE 2018

COLLAPSE RESISTANCE OF A STEEL FRAME WITH HIGH POST-YIELD STIFFNESS STAINLESS STEEL DEVICES IN ABAQUS

Marco BAIGUERA[1], George VASDRAVELLIS[2], Theodore L. KARAVASILIS[3]

ABSTRACT

The collapse resistance of a dual seismic-resistant steel frame with high post-yield stiffness stainless steel devices is evaluated. The dual system consists of a moment-resisting frame equipped with dissipative concentric braces. The dissipative braces are realised as the in-series connection of stainless steel pins (SSPs) with a hourglass shape, conventional steel braces, and friction pads. The latter are activated only under very large seismic intensities to control the peak force of the braces. Moreover, replaceable ductile fuses are used in the beams at the expected locations of plastic hinges. Incremental dynamic analyses are performed using an advanced finite element model in Abaqus that simulates geometric and material nonlinearities including ductile fracture in the SSPs. The cyclic behaviour of the SSPs is experimentally evaluated by testing two full-scale specimens in a configuration reproducing their actual connection details in the steel frame. The results of fourteen cyclic tests show that the SSPs have stable symmetric hysteresis, high post-yield stiffness, and large energy dissipation and fracture capacities. Ductile fracture in SSPs is modelled using a plastic motion-based criterion that is calibrated against the experimental results. The results of incremental dynamic analyses show that the proposed system has superior resistance against seismic collapse, with a 1.2% collapse probability under the maximum-considered earthquake. The large collapse capacity is due to the high post-yield stiffness and the excellent fracture capacity of the SSPs. In particular, fracture is detected only under two long duration earthquakes scaled to intensities higher than that of the maximum considered earthquake.

Keywords: Seismic collapse; Stainless steel seismic device; Energy dissipative brace; Ductile fracture.

1. INTRODUCTION

Conventional seismic-resistant steel frames designed in accordance to modern codes perform well under strong earthquakes by preventing collapse and ensuring life safety. However, in major seismic events, these systems may experience extensive inelastic deformations in main structural members and significant residual drifts, causing downtime and significant socio-economic losses. Innovative resilience-based seismic design approaches have recently been proposed to mitigate the limitations of conventional steel frames.

An effective strategy to overcome the issue of damage is to isolate plastic deformations in few easy to inspect and replace structural elements. Replaceable connection elements for steel moment-resisting frames (MRFs) were proposed by Balut and Gioncu (2003), Castiglioni et al. (2012), and Shen et al. (2013). In braced frames, yielding metallic devices have been used to avoid damage in main structural members and increase the energy dissipation capacity. Based on the first concepts developed in New Zealand in the 1970s (Kelly et al. 1972, Skinner et al. 1975), a wide range of steel yielding devices were proposed. Among these, plates and bars with a variable cross-section that follows the bending moment diagram were developed to provide a uniform yielding, and therefore, avoid localised deformations. Devices made of multiple steel plates, such as the added damping and stiffness (ADAS) flexural-beam damper (Whittaker et al. 1989), were implemented in either eccentrically or

[1]PhD Candidate, IIE, Heriot-Watt University, Edinburgh, United Kingdom, mb311@hw.ac.uk
[2]Assistant Professor, IIE, Heriot-Watt University, Edinburgh, United Kingdom, G.Vasdravellis@hw.ac.uk
[3]Professor, Faculty of Engineering, University of Southampton, United Kingdom, T.Karavasilis@soton.ac.uk

concentrically braced frames. A triangular version of ADAS, known as T-ADAS, was proposed by Tsai and Li (1993). Similarly, hourglass-shaped or single-tapered bars were used in proprietary energy-dissipating systems (Kajima 1991). Other similar concepts implemented in concentrically-braced frames (CBFs) include those proposed by Vayas and Thanopoulos (2005) and Gray et al. (2014). Although effective in dissipating seismic energy, the aforementioned yielding devices do not control residual drifts, i.e. a response parameter that influences downtime and repair costs in the aftermath of a strong earthquake.

Residual drifts can be effectively minimised by using post-tensioning technology that provides self-centering capability. For example, self-centering MRFs use post-tensioned tendons to clamp the beams to columns while allowing for gap opening in the beam-column interface. Several configurations of self-centering MRFs have been proposed, with the main difference being the type of energy-dissipation device used, i.e. yielding based (Ricles et al. 2001, Christopoulos et al. 2002, Chou et al. 2006, Vasdravellis et al. 2013) or friction based (Rojas et al. 2005, Tsai et al. 2008). Post-tensioning technology has also been applied to braced systems (Christopoulos et al. 2008, Roke et al. 2009). However, implementing such systems in current practice can be challenging, since they involve additional complexity in design, fabrication and erection (Chancellor et al. 2014).

A valid alternative to post-tensioning is increasing the high post-yield stiffness of the structure, which can be achieved by introducing a secondary elastic frame in parallel with the primary frame, i.e. a dual system (Pettinga et al. 2008). Alternatively, Baiguera et al. (2016) have proposed a dual system that consists of an MRF equipped with dissipative concentric braces, denoted as dual CBF-MRF. The dissipative braces are realised as the in-series connection of stainless steel pins (SSPs) with a hourglass shape, conventional steel braces, and friction pads. Nonlinear dynamic analyses showed that the high post-yield stiffness of the SSPs combined with the elastic capacity of the MRF result in negligible residual drifts under the design basis earthquake (DBE, probability of exceedance 10% in 50 years) and very small residual drifts under the maximum considered earthquake (MCE, probability of exceedance 2% in 50 years).

This paper focuses on the collapse assessment of the proposed dual CBF-MRF. The results of fourteen cyclic tests on full-scale SSPs are presented. The collapse performance of the dual CBF-MRF is evaluated using advanced models in Abaqus (Dassault Systèmes 2014). A plastic motion–based damage criterion was calibrated to the experimental results to explicitly simulate ductile fracture of the SSPs. The results of incremental dynamic analysis (IDA) (Vamvatsikos and Cornell 2002), where the frame is subjected to a set of 24 ground motions scaled to trigger collapse, are presented. The influence of ground motion duration is also investigated.

2. PROPOSED DUAL CBF-MRF

Figure 1a shows the configuration of the dual CBF-MRF proposed in Baiguera et al. (2016). The SSPs are installed at one end of the braces and pass through aligned holes between the gusset plate welded to the beam and column and a strong U-shaped plate connected by either welding or bolting to the brace member (Figure 1b). SSPs dissipate energy due to inelastic deformations produced mainly by bending. The hourglass shape of the SSPs promotes a constant curvature profile and a uniform distribution of plastic deformations to delay fracture and increase energy dissipation. Replaceable fuses are placed in the main beams immediately after the gusset plates, where plastic hinges are expected to develop. They are designed following the same concept of the replaceable link proposed by Shen et al. (2011). The fuses are I-sections smaller than the main beam, and are welded on strong end-plates bolted to the main beam. To meet capacity design requirements and avoid undesirable column failure due to high post-yield stiffness of the SSPs, friction pads are placed between the brace members and the beam gusset plate at the top of each floor (Figure 1a). The friction pads are activated at a predefined story drift level.

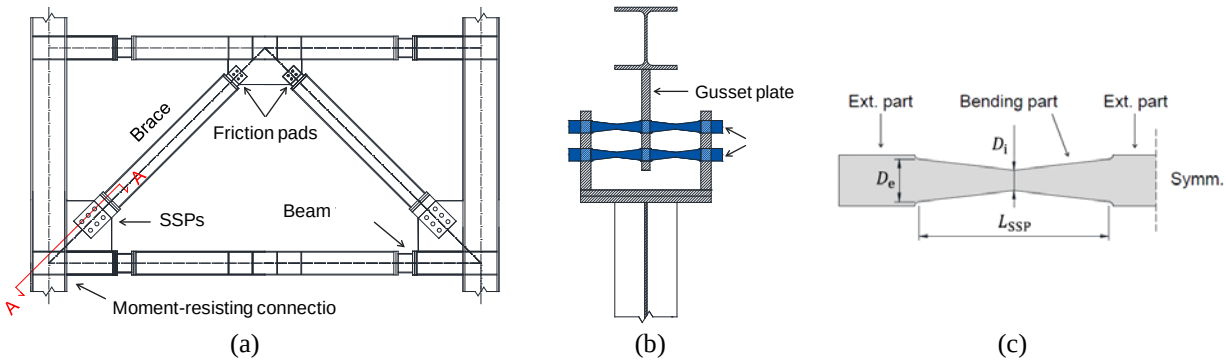

(a) (b) (c)

Figure 1: (a) Geometry of the dual CBF-MRF; (b) brace-to-SSP connection detail; (c) geometry, deflection, elastic bending moment, and shear diagram of a SSP.

SSPs are made of two hourglass-shaped bending parts. The geometric properties of the bending part are shown in Figure 1c. The internal bending parts have length L_{SSP}, maximum diameter D_e, and minimum diameter D_i at mid-length. The static system for the bending part assumes that the maximum plastic moment M_{pl} is halfway between D_e and D_i, as follows:

$$M_{pl} = \frac{{D_{PH}}^3}{6} f_{y,SSD} \tag{1}$$

where $D_{PH} = (D_e + D_i)/2$ and $f_{y,SSD}$ is the yield strength of duplex stainless steel (SSD). The yield force $F_{y,SSP}$ of a SSP is then calculated as:

$$F_{y,SSP} = \frac{4M_{pl}}{L_{PH}} = \frac{2{D_{PH}}^3}{3L_{PH}} f_{y,SSD} \tag{2}$$

where $L_{PH} = L_{SSP}/2$. As described in detail in Vasdravellis et al. (2014), the elastic stiffness K_{SSP} of a SSP is given by:

$$K_{SSP} = 2\beta \frac{9\pi D_e^3 D_i EG}{(40ED_e^2 L_{SSP} + 48GL_{SSP}^3)} \tag{3}$$

where E is the modulus of elasticity and G is the shear modulus of the SSP material. β is a parameter that accounts for the additional flexibility due to local yielding in the supporting plates and is equal to 0.5.

In the proposed system, a defined number of SSPs (n_{SSP}) working in parallel to each other are placed in series with the brace, and therefore, the yield force $F_{y,tot}$ and the global stiffness K_{tot} of the energy-dissipating braces are calculated as follows:

$$F_{y,tot} = n_{SSP} \cdot F_{y,SSP} \tag{4}$$

$$\frac{1}{K_{tot}} = \frac{1}{K_{SSPs}} + \frac{1}{K_{brace}} = \frac{1}{n_{SSP} \cdot K_{SSP}} + \frac{1}{\frac{EA_{brace}}{L_{brace}}} \tag{5}$$

where K_{SSPs} is the stiffness of all WHPs, and K_{brace} is the axial stiffness of the bracing member having length L_{brace} and cross-sectional area A_{brace}. The above equations were applied in Baiguera et al. (2016) for the design of a 6-storey prototype building as the proposed dual CBF-MRF. The frame was designed to have similar strength and stiffness of a conventional MRF with buckling-restrained braces (BRBs), in accordance with Eurocodes 3 and 8 (EC3 2003, EC8 2004).

3. EXPERIMENTAL TESTS

3.1 Specimens and test apparatus

Two different full-scale SSP geometries, representing the devices of the third and sixth story of the prototype building in Baiguera et al. (2016), were tested. The two geometries are denoted as SSP1 and SSP2, respectively. Since SSPs undergo the same displacement when loaded, tests were conducted on a single SSP for each connection. Figure 2a shows the geometries of the two full-scale specimens. SSP1 has D_e = 50 mm, D_i = 24 mm, and L_{SSP} = 225 mm, while SSP2 has the same length of SSP1, but smaller diameters (D_e = 40 mm and D_i = 18 mm). Seven specimens of each geometry were manufactured by machining 740-mm-long round bars made of duplex stainless steel ($f_{y,SSD}$ = 520 MPa). The specimens were fabricated with a clearance of 0.2 mm between their external surfaces and the holes of the supporting plates.

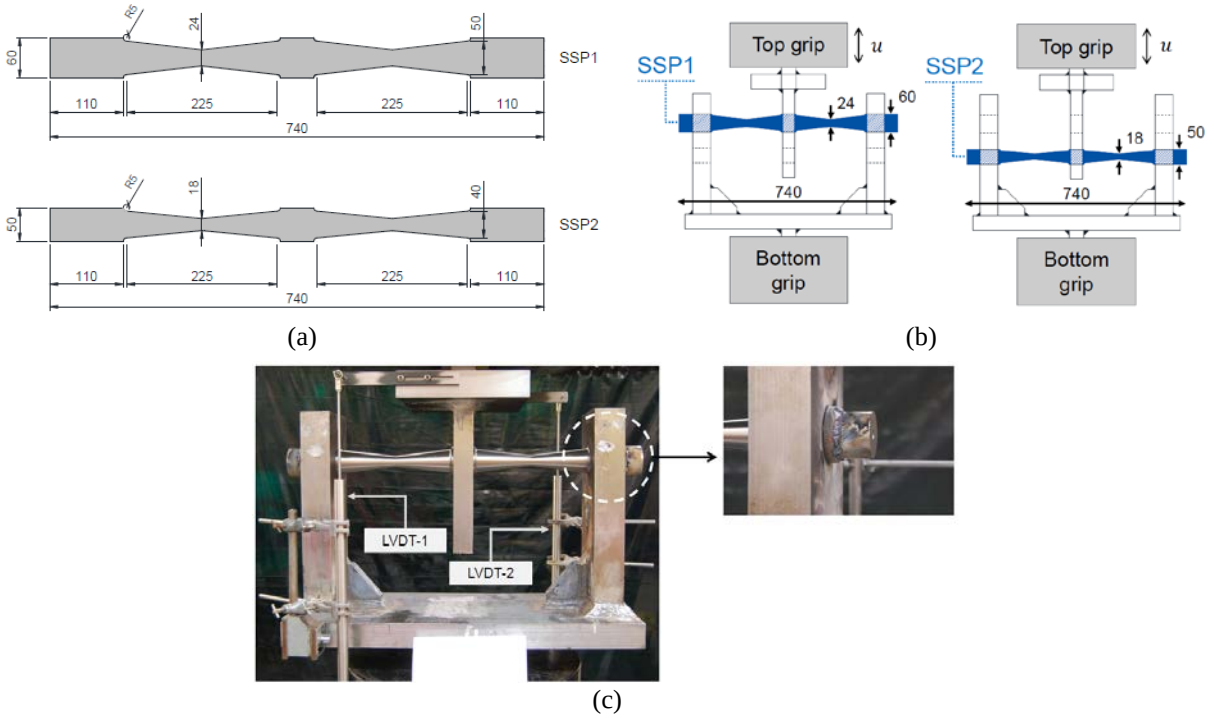

Figure 2: (a) Geometry of the full-scale SSP specimens; (b) testing configuration for SSP1 and SSP2; (c) testing instrumentation and detail with steel collar welded onto SSP1.

The full-scale component tests were performed using a self-reacting testing machine with 2000 kN force capacity in tension and compression and ±120 mm displacement capacity. Figures 2b-c shows the test setup, which reproduces the SSP-brace connection and designed to accommodate the two different SSP geometries. Each specimen was inserted into aligned holes that were drilled on vertical plates welded to 50-mm thick horizontal plates. The top row of holes was used for SSP1, whereas the bottom row for SSP2. The minimum thickness of the supporting plates was selected according to the design rules presented in Vasdravellis et al. (2014). Two linear variable differential transformers (LVDTs) were used to measure the relative displacement between the top and bottom assemblies. The SSPs were axially constrained using a 10-mm thick steel collar welded onto their ends (Figure 2c). At the start of each test, the collar was just in contact with the vertical plates.

The SSPs were subjected to a range of different loading protocols, which are listed in Table 1. The first loading protocol is the one recommended in Annex K of ANSI/AISC 341-10 (2010) for the seismic evaluation of BRBs. The response of SSPs was also evaluated under ultra-low cycle fatigue, which is a failure expected under earthquakes due to a relatively small number of cycles of large inelastic deformations, generally less than 100 (Pereira et al. 2014) or even 20 (Kanvinde et al. 2007). To investigate ductile fracture of SSPs, constant amplitude (CA) and random protocols were used. The

imposed CA amplitudes were defined as multiples of the SSP yield displacement, i.e., u_y = 7 mm. The random protocols consist of randomly-generated number of cycles and imposed displacements. These protocols were defined assuming displacement values in the range of 2 to 8 times u_y and cycles between 1 and 9. The loading protocols were applied under displacement control at a rate ranging from 5 to 40 mm/min at ambient temperature.

Table 1. Test matrix of the full-scale tests on SSPs

Specimen	**Test**	**Protocol**	**Fracture initiation** (cycle no.)	**20 pc strength loss** (cycle no.)	**Full fracture** (cycle no.)
SSP1	1	AISC	-	-	-
	2	CA = $7u_y$	21	27	28
	3	CA = $6u_y$	25	34	35
	4	CA = $5u_y$	31	42	43
	5	CA = $4u_y$	43	73	78
	6	Random-1	35	58	59
	7	Random-2	25	44	45
SSP2	8	AISC	-	-	-
	9	CA = $8u_y$	30	33	33
	10	CA = $7u_y$	36	42	43
	11	CA = $6u_y$	41	54	59
	12	CA = $5u_y$	45	68	76
	13	CA = $4u_y$	54	83	89
	14	Random	40	46	48

3.2 Test results

Figure 3a shows the force-displacement hysteresis of SSP1 under the AISC loading protocol. SSP1 successfully passed the imposed protocol showing stable hysteresis and large ductility. No cracks or signs of deterioration were observed. Figure 3b illustrates the deformed shape of SSP1 under the AISC test. SSP2 exhibited a similar response under the same protocol. Figure 3c-d shows the force-displacement curve of SSPs under CA = $7u_y$. The force-displacement curves are characterized by slight pinching at zero force, due to the clearance that allows the pins to slip. In addition, there is a noticeable hardening behaviour at large displacements (u > ±40 mm).

Ductile fracture consistently initiated on the surface of the SSP at the middle sections of the bending parts, i.e. halfway between D_e and D_i, as illustrated in Figure 3e-f. These fracture locations are denoted as section 1 and 2, where section 1 is the one closest to the lower supporting plate. The fracture mechanism confirms the analytical assumption that plastic hinges form in the middle of the half bending part. Using Eqs. (1-2), F_{SSP1} is equal to 156 kN and F_{SSP2} is equal to 75 kN, i.e. in excellent agreement with the corresponding experimental values, i.e. 150 kN and 75 kN. The number of cycles to fracture initiation and full-section failure were recorded for each ULCF test, as reported in Table 1. Once fracture initiation occurred in sections 1 and 2, several micro-cracks gradually propagated to full-section fracture. Figure 3g shows the evolution of ductile fracture in SSP1 tested under CA = $6u_y$. Cracks were first observed after 25 cycles, followed by the growth of larger crack during the 29th cycle, which propagated in the successive six cycles up to the full-section fracture of the specimen. Following fracture initiation, the load-carrying capacity of the SSPs remained stable for many cycles, and dropped by 20% just few cycles before failure, as listed in Table 1.

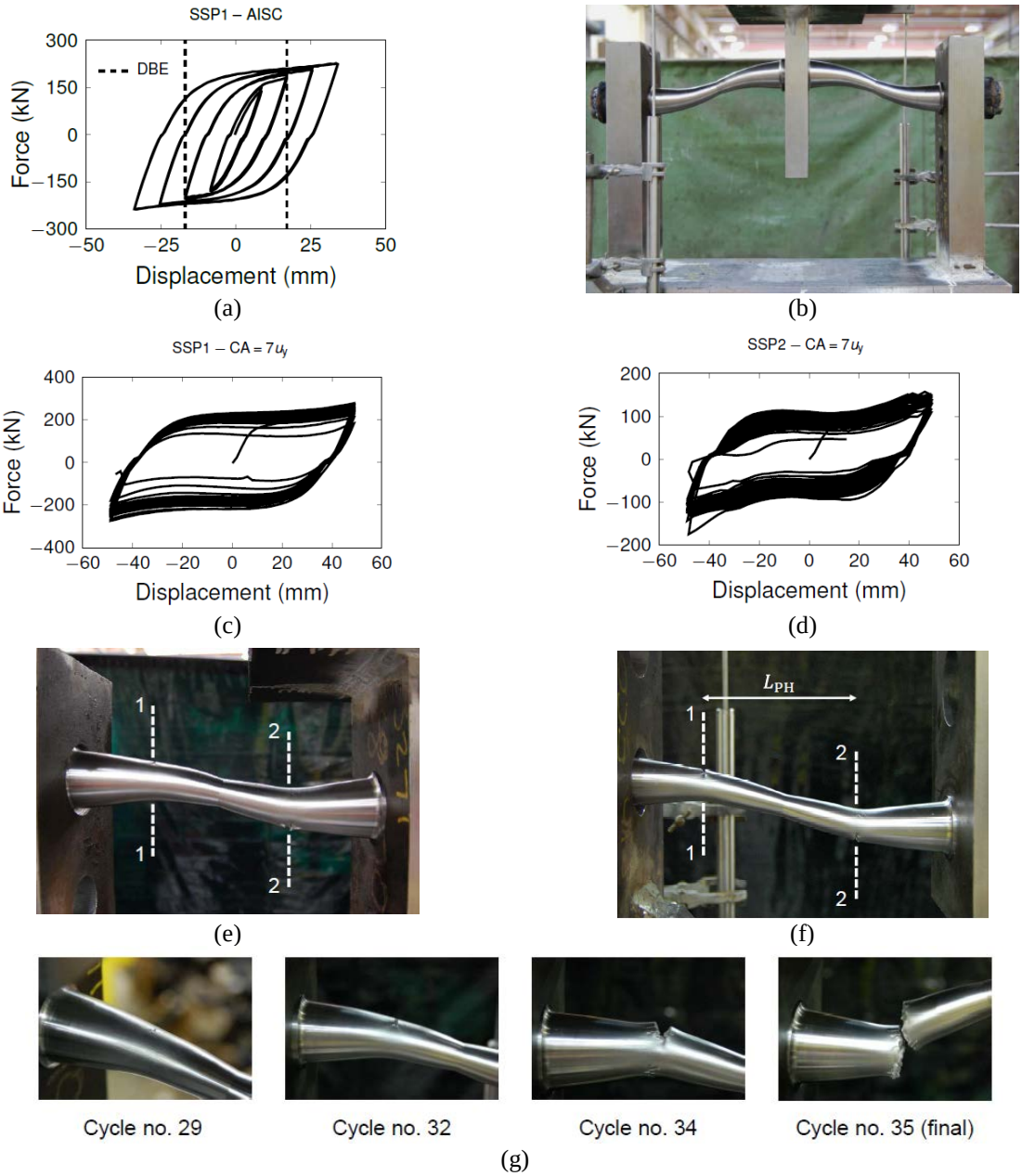

Figure 3: (a) Hysteresis of SSP1 under the AISC protocol; (b) deformed shape of SSP1; (c) and (d) hystereses of SSP1 and SSP2 under CA = $7u_y$; (e) and (f) fracture locations in SSP1 and SSP2; and (g) ductile fracture initiation and evolution in SSP1 under CA = $6u_y$

4. COLLAPSE POTENTIAL ASSESSMENT

The seismic collapse resistance of the dual CBF-MRF was evaluated using the prototype frame designed in Baiguera et al. (2016). IDA were conducted on a FEM model of the steel frame that explicitly simulates ductile fracture of SSPs.

4.1 Prototype building

The 6-storey prototype building in Baiguera et al. (2016) was used. Since the original design of the dual frame had five different SSP geometries over the six storeys, a revised design was developed using only the two experimentally-tested SSP geometries. Following the design methodology presented in Section 2, the energy-dissipating braces were designed using either SSP1 or SSP2, while

maintaining similar yield force $F_{y,tot}$ and global stiffness K_{tot} to the original CBF-MRF design. As reported in Table 2, the SSP1 geometry is used for storeys 1 to 4, while SSP2 for the top storeys 5 and 6. The beam, column and brace sections are the same as in the original design. The fundamental period of vibration of the revised CBF-MRF is 0.78 s, comparable to that of the original frame (i.e., 0.75 s).

Table 2. Design details of the dual CBF-MRF

Storey	**Column**	**Beam**	**Brace**	n_{SSP}	D_e (mm)	D_i (mm)	L_{SSP} (mm)	$F_{y,tot}$ (kN)	K_{tot} (N/mm)
6	HEB400	IPE330	HEA300	4	40	18	225	300	44,000
5	HEB400	IPE330	HEA300	5	40	18	225	375	55,000
4	HEB400	IPE330	HEA300	4	50	24	225	600	80,000
3	HEB400	IPE330	HEA300	4	50	24	225	600	80,000
2	HEB500	IPE330	HEA300	5	50	24	225	750	100,000
1	HEB500	IPE330	HEA300	5	50	24	225	750	100,000

4.2 Nonlinear FEM model of the dual CBF-MRF

The FEM model of the dual CBF-MRF developed in Abaqus for nonlinear time-history analyses in Baiguera et al. (2016) was used. As illustrated in Figure 4, beams and columns were modelled using beam elements, while the SSPs and friction pads using nonlinear connector elements. More details about the FEM modelling are provided in Baiguera et al. (2016). The hysteretic behaviour of the connectors modelling the SSPs was defined using an elastoplastic force-displacement law. The inelastic response of a connector is given by the SSPs working in parallel to each other. The results of the full-scale tests were used to calibrate the half-cycle input data for a single SSP. Figures 5a shows the comparison of the connector force-displacement responses with the experimental hysteresis of SSP1 under CA = $7u_y$. It should be noted that connector elements are not capable of capturing three-dimensional effects, such as the pinching effect at zero force.

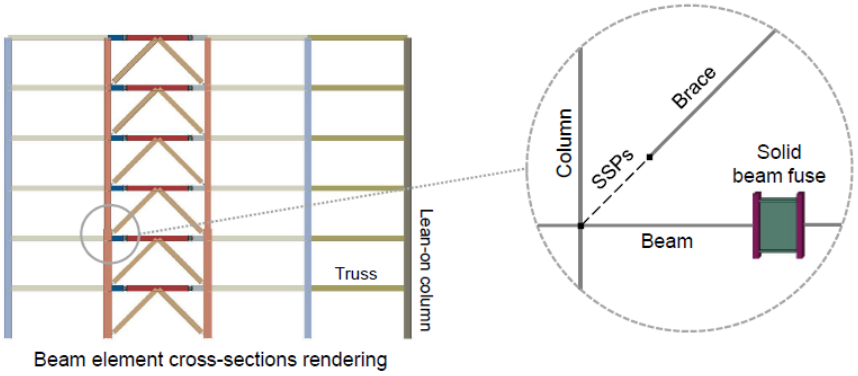

Figure 4: View of the simplified FEM model of the dual CBF-MRF

The beam-solid model is capable of simulating the mechanisms that can lead to collapse under extreme ground motions, including the P-Δ effects from the gravity frame, the deterioration of the beam fuses due to local buckling, and fracture of SSPs. To simulate ductile fracture, a plastic motion-based damage criterion that degrades the elastic-plastic response in the connector elements modelling the SSPs was used. Ductile fracture is tracked using the cumulative plastic displacement $\bar{u}^{pl}$. The connector fracture model assumes that fracture initiates in a SSP when the following condition is satisfied:

$$D_0 = \frac{\bar{u}^{pl}}{\bar{u}_0^{pl}} \tag{6}$$

where D_0 is the connector fracture initiation index, and $\bar{u}_0^{pl}$ is the equivalent relative plastic motion at fracture initiation. Following initiation, the force response of the connector deteriorates as follows:

$$F = F_{\text{eff}} \cdot (1 - d_{\text{evol}}) \tag{7}$$

where d_{evol} is the damage connector evolution variable and F_{eff} is the response of the connector without degradation (Dassault Systèmes 2014). To accurately trace the degradation of the force response of the SSPs, the damage evolution criterion was defined as a tabular function of the difference between the equivalent plastic displacements at failure ($\bar{u}_{\text{f}}^{pl}$), 20% loss in the force-carrying capacity ($\bar{u}_{20}^{pl}$), and fracture initiation ($\bar{u}_0^{pl}$). The damage evolution law was calibrated against the experimental tests. The $\bar{u}^{pl}$ values at the considered three limit states were identified for each test by extracting the history of the corresponding output variable, denoted as CUPEQ in Abaqus, from analyses on a single connector element. Figure 5b shows the comparison between the experimental and connector force histories for SSP1 under CA = $7u_{\text{y}}$, indicating that the calibrated connectors are capable of accurately tracing the degradation of the force response. Figure 5c plots the plastic motion laws obtained from all the ULCF tests on SSP1. It should be noted that $\bar{u}_0^{pl}$ value fall into a relatively small range, while a larger deviation from the mean value is observed for $\bar{u}_0^{pl}$ and $\bar{u}_{\text{f}}^{pl}$ values. A similar trend was observed for SSP2. The minimum $\bar{u}^{pl}$ were conservatively used for the collapse assessment of the dual CBF-MRF. Figure 5d plots the base shear coefficient versus *V/W* (i.e. base shear *V* normalised by the seismic weight *W*) versus roof drift response from a nonlinear static pushover analysis on the dual CBF-MRF. The connectors modelling the friction pads were calibrated so that they are activated at a roof storey drift of 3%.

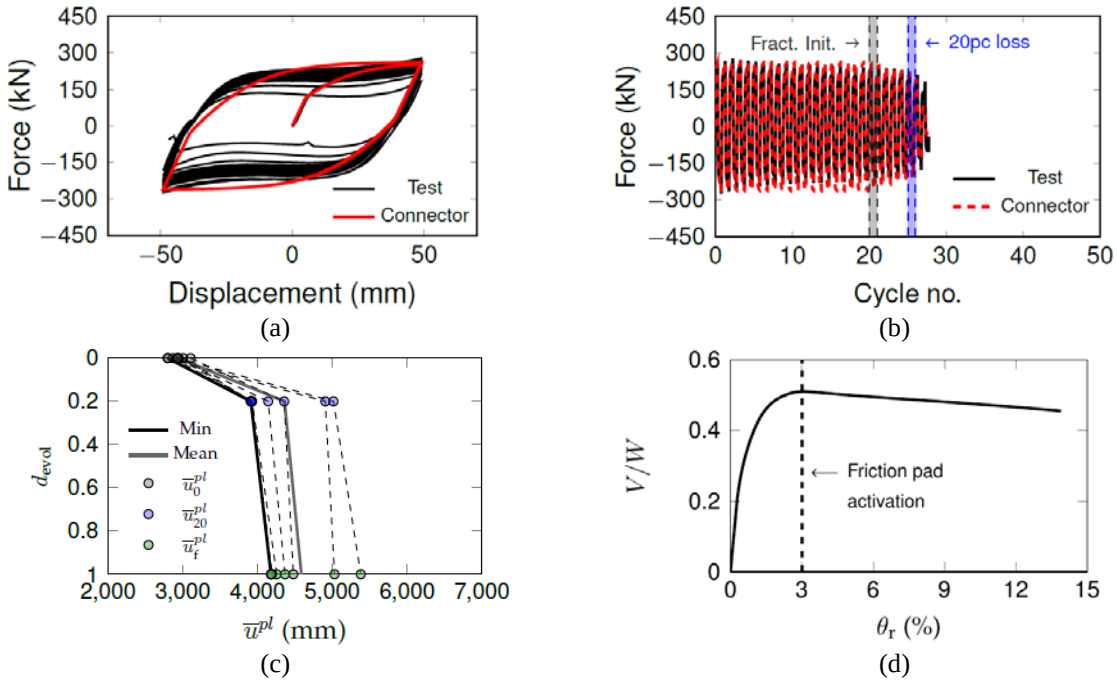

Figure 5: Connector calibration: (a) experimental-connector hysteresis of SSP1 (CA = $7u_{\text{y}}$); (b) experimental-connector force responses of SSP1 (CA = $7u_{\text{y}}$); (c) calibrated fracture evolution laws for SSP1; and (d) base shear-roof drift response of the dual CBF-MRF.

4.3 Incremental dynamic analyses

The set of 22 ground motion records developed in FEMA P695 (2008) were used for IDA. To study the influence of ground motion duration on the dynamic response of the CBF-MRF, two additional records were selected from Ruiz-Garcia (2010), i.e. Valparaiso El Amendral (Chile 1985) and Michoacan La Villita (1976). This study employs the first-mode spectral acceleration $S_a(T_1)$ as the seismic intensity measure (IM) and the maximum peak inter-storey drift $\theta_{s,max}$ as the engineering demand parameter (EDP). To reduce the computational effort, $S_a(T_1)$ is systematically scaled up in increments equal to $0.5S_{a,MCE}(T_1)$, i.e. half the intensity at the MCE hazard level. For the dual CBF-MRF, $S_{a,MCE}(T_1)$ = 1.04 g. To investigate the response near to collapse, smaller increments are applied. The collapse evaluation of the dual CBF-MRF subjected to a total of 24 ground motions involved over 250 analyses. To determine the collapse intensity $S_{a,col}(T_1)$ for each of the 24 records, a combination of collapse capacity criteria was used. Generally, these criteria can be either IM- or EDP-based (Vamvatsikos & Cornell 2002). This study assumes the following limit state rules: the 20% tangent slope IM-based approach and the EDP limit corresponding to $\theta_{s,max}$ = 10%. The IDA curves for the 24 ground motions are shown in Figure 6a, where each data point represents the $S_a(T_1)$ normalised to $S_{a,MCE}(T_1)$ and the recorded $\theta_{s,max}$

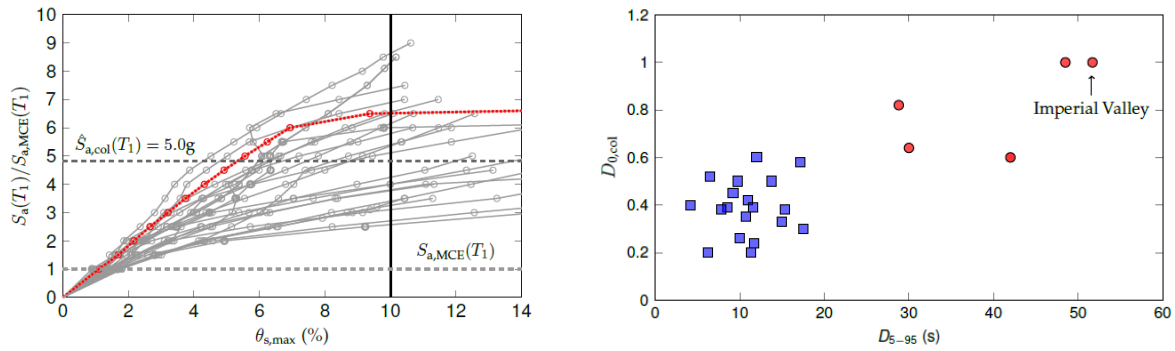

Figure 6: Incremental dynamic analysis (IDA) using 24 ground motions: (a) IDA curves; and (b) significant motion duration vs. ductile fracture initiation index

The IDA results for the 1979 Imperial Valley (Delta) earthquake are presented above. The IDA curve for the considered ground motion is highlighted in red in Figure 6a. Straight lines are drawn between consecutive point data. The slope of the line between the origin and the first point defines the elastic stiffness of the IDA curve. When the curve rapidly flattens out, it reaches a plateau that indicates dynamic instability of the structure.

Recent studies have shown that the nonlinear response of structural systems subjected to cumulative damage is affected by ground motion duration-related parameters (Iervolino et al. 2006). Different approaches can be used to evaluate duration. A widely-accepted parameter is the significant motion duration, defined as the time interval during which a certain amount of energy is dissipated (Trifunac and Brady 1975). Energy is measured using the Arias intensity I_A (Arias 1970). A commonly-used significant motion duration parameter is $D_{5\text{-}95}$, which is defined as the time interval between the 5% and 95% of I_A. Based on the approach by Ruiz-Garcia (2010), records were classified in short duration, i.e. $D_{5\text{-}95}$ = 0-17.5 s, and long duration, i.e. $D_{5\text{-}95}$ = 28.8-51.7 s. Out of the 22 records selected from FEMA P695 (2008), three are long duration motions, including the 1979 Imperial Valley (Delta) ground motion, and the remaining are short duration, while the two additional records from Ruiz-Garcia (2010) are both long duration. To characterise the scale of fracture reached in the SSPs under the earthquake records, a fracture initiation index at collapse $D_{0,col}$ was calculated as the ratio between the $\bar{u}^{pl}$ value recorded at collapse and the corresponding $\bar{u}_0^{pl}$ value. The distribution of the $D_{5\text{-}95}$- $D_{0,col}$ parameters, plotted in Figure 6b, shows a large record-to-record variability. Fracture initiation ($D_{0,col}$ = 1), occurred only under two out of the 24 ground motions, including 1979 Imperial Valley (Delta) record. While $D_{0,col}$ values for short records are in the range of 0.2-0.6, long duration earthquakes

determine a much smaller safety margin against fracture, where the corresponding $D_{0,col}$ is in the range 0.6-1.

The $S_{a,col}(T_1)$ data were then used to probabilistically assess the collapse capacity. The resulting probability of collapse versus ground motion intensity $S_a(T_1)$ relationship for the 24 ground motions is plotted as point data in Figure 7a. A collapse fragility curve was obtained by fitting a lognormal distribution to the $S_{a,col}(T_1)$ values, which are ranked in ascending order. It was found that the safety margin against collapse, defined as the ratio of the median $S_{a,col}(T_1)$ to $S_{a,MCE}(T_1)$, is equal to 4.81. The slope of the fragility curve is defined by the lognormal standard deviation β_{RTR} = 0.35, which represents the record-to-record uncertainty. To account for further sources of uncertainty, a total collapse uncertainty β_{tot} = 0.7, which is consistent with the range identified by studies on modelling uncertainty (Liel et al. 2009), was assumed. Figure 7b illustrates the collapse probability for $S_{a,col}(T_1)$ values normalised by $S_{a,MCE}(T_1)$, using β_{RTR} and β_{tot}. Based on the fragility curve with β_{tot}, the CBF-MRF has 1.2% collapse probability at the MCE level, which is largely below the 10% probability limit defined by FEMA P695 (2008). This indicates an excellent collapse performance of the proposed dual CBF-MRF.

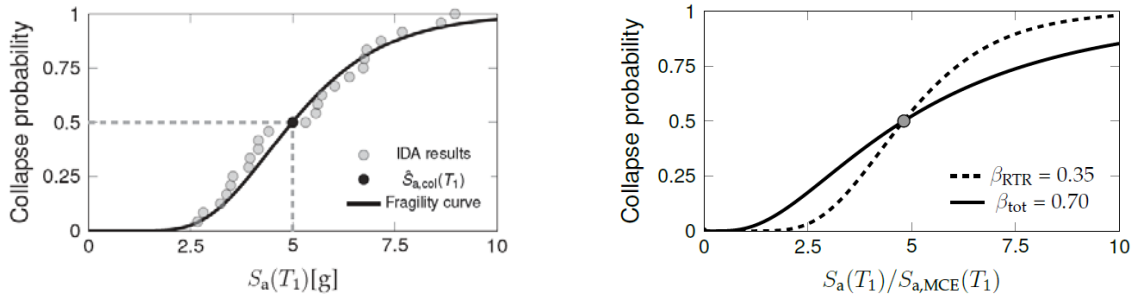

Figure 7: (a) Collapse fragility curves of the CBF-MRF fitted through IDA results; and (b) fragility curves of the CBF-MRF relative to record-to-record variability and to total collapse uncertainty

5. CONCLUSIONS

Duplex stainless steel pins (SSPs) with hourglass shape were used in a dual CBF-MRF frame to reduce residual drifts by taking advantage of their high post-yield stiffness. The SSPs were experimentally validated by means of full-scale components tests. The experimental results were used to calibrate nonlinear models capable of simulating the cyclic behaviour of SSPs up to fracture. IDA were employed to assess the collapse potential of the CBF-MRF. Based on the results presented in this paper, the following conclusions are drawn:

- SSPs possess excellent ductility and large energy dissipation capacity under ultra-low cycle fatigue loading.
- Fracture initiates on the surface of the SSP at the middle sections of the bending parts. Following initiation, the SSPs can endure several cycles to full-section fracture, without significant degradation in their force-carrying capacity.
- By accounting for the record-to-record variability and modelling uncertainty, the dual CBF-MRF has a 1.2% collapse probability at the MCE level, which is largely below the permissible limit of 10% set in FEMA P695 (2008).
- Under most of the earthquake records used in IDA, the safety margin against fracture in the SSPs was considerable. Fracture occurred only for two ground motions having a long significant duration, i.e., severe energy dissipation demand.

6. ACKNOWLEDGMENTS

This research was supported by the Engineering and Physical Sciences Research Council (EPSRC) of

the United Kingdom (Studentship Ref: 1880024). The authors acknowledge Mr David Reichardt for his help during the lab experiments, and the valuable assistance of the technical staff of the Heavy Structures Lab at Heriot-Watt University, Mr. Tom Ferguson, Mr. Tom Stenhouse, Mr. David Murray and Mr. Alastair MacFarlane.

7. REFERENCES

ANSI/AISC 341/10 (2010). Seismic provisions for structural steel buildings, AISC, Chicago.

Arias A (1970). *A measure of earthquake intensity*. Seismic Design for Nuclear Power Plants, MIT Press, Cambridge, MA.

Baiguera M, Vasdravellis G, Karavasilis TL (2016). Dual seismic-resistant steel frame with high post-yield stiffness energy-dissipative braces for residual drift reduction. *Journal of Constructional Steel Research*, 122: 198-212.

Balut N, Gioncu V (2003). Suggestion for an improved 'dog-bone' solution, *Proceedings of STESSA 2003: Behaviour of Steel Structures in Seismic Areas*, 129-134, Balkema, Lisse, Netherlands.

Castiglioni CA, Kanyilmaz A, Calado L (2012). Experimental analysis of seismic resistant composite steel frames with dissipative devices. *Journal of Constructional Steel Research*, 76:1-12.

Chancellor, N. B., Eatherton, M. R., Roke, D. A. & Akbas, T. (2014). Self-centering seismic lateral force resisting systems: High performance structures for the city of tomorrow. *Buildings*, 4(3):520-548.

Chou C-C, Chen J-H, Chen Y-C, Tsai K-C (2006). Evaluating performance of post-tensioned steel connections with strands and reduced flange plates. *Earthquake Engineering & Structural Dynamics*, 35:1167-1185.

Christopoulos C, Filiatrault A, Uang C-M, Folz B (2002). Posttensioned energy dissipating connections for moment-resisting frames. *Journal of Structural Engineering*, 128(9):1111-1120.

Christopoulos C, Tremblay R, Kim H, Lacerte M (2008). The selfcentering energy dissipative (SCED) bracing system for the seismic resistance of structures. *Journal of Structural Engineering*, 134(1):96-107.

Dassault Systèmes (2014). ABAQUS documentation, 6.14 edn, Dassault Systèmes Simulia, Providence, RI.

EC3 (2003). Eurocode 3: Design of steel structures, Part 1.1: General Rules and Rules for Building. *European Committee for Standardization*, CEN, Brussels.

EC8 (2004). Eurocode 8: Design Provisions for Earthquake Resistance of Structures, Part 1: General Rules, Seismic Actions and Rules for Building. *European Committee for Standardization*, CEN, Brussels.

FEMA P695 (2008). Quantification of building seismic performance factors, Federal Emergency Management Agency, CA.

Gray MG, Christopoulos C, Packer JA (2014). Cast steel yielding brace system for concentrically braced frames: Concept development and experimental validations. *Journal of Structural Engineering*, 140(4):04013095.

Kajima (1991). Honeycomb Damper System, Kajima Corporation, Japan.

Kanvinde AM, Deierlein GG (2007). Cyclic void growth model to assess ductile fracture initiation in structural steels due to ultra low cycle fatigue. *Journal of Engineering Mechanics*, 133(6):701-712.

Kelly JM, Skinner RI, Heine AJ (1972). Mechanisms of energy absorption in special devices for use in earthquake-resistant structures. *Bulletin of the New Zealand Society of Earthquake Engineering*, 5(3):63-88.

Iervolino I, Manfredi G, Cosenza E (2006). Ground-motion duration effects on nonlinear seismic response. *Earthquake Engineering and Structural Dynamics*, 35(1):21-38.

Liel A, Haselton C, Deierlein G, Baker J (2009). Incorporating modelling uncertainties in the assessment of seismic collapse risk of buildings. *Structural Safety*, 31(2):197-211.

Pereira J, de Jesus A, Xavier J, Fernandes A (2014). Ultra low-cycle fatigue behaviour of a structural steel. *Engineering Structures*, 60:214-222.

Pettinga D, Christopoulos C, Pampanin S, Priestley MJN (2008). Effectiveness of simple approaches in mitigating residual deformations in buildings. *Earthquake Engineering & Structural Dynamics*, 36(12):1763-1783.

Ricles JM, Sause R, Garlock M, Zhao C (2001). Posttensioned seismic-resistant connections for steel frames, *Journal of Structural Engineering*, 127(2):113-121.

Rojas P, Ricles JM, Sause R (2005). Seismic performance of post-tensioned steel moment resisting frames with friction devices. *Journal of Structural Engineering*, 131(4):529-540.

Roke D, Sause R, Ricles JM, Gonner N (2009). Design concepts for damage-free seismic-resistant self-centering steel concentrically braced frames. *Structures 2009*, ASCE, 1421-1430, Austin, Texas.

Ruiz-Garcia J (2010). On the influence of strong-ground motion duration on residual displacement demands. *Earthquakes and Structures*, 1(4):327-344.

Shen Y, Christopoulos C, Mansour N, Tremblay R (2011). Seismic design and performance of steel moment-resisting frames with nonlinear replaceable links. *Journal of Structural Engineering*, 137(10):1107-1117.

Skinner RI, Kelly JM, Heine AJ (1975). Hysteretic dampers for earthquake-resistant structures. *Earthquake Engineering & Structural Dynamics*, 3(3):287-296.

Trifunac M, Brady A (1975). A study on the duration of strong earthquake ground motion. *Bulletin of the Seismological Society of America*, 65:581-626.

Tsai K-C, Chou C-C, Lin CL, Chen PC, Jhang, SJ (2008). Seismic self-centering steel beam-to-column moment connections using bolted friction devices. *Earthquake Engineering & Structural Dynamics*, 37(4):627-645.

Tsai K-C, Li JW (1994). Seismic analysis of passive energy dissipation subsystems by hybrid experiments, *Proceedings of the 12th International Modal Analysis Conference*, 1520-1526, Honolulu, Hawaii.

Vamvatsikos D, Cornell CA (2002). Incremental dynamic analysis. *Earthquake Engineering & Structural Dynamics*, 31(3):491-514.

Vasdravellis G, Karavasilis TL, Uy B (2013). Large-scale experimental validation of steel post-tensioned connections with web hourglass pins. *Journal of Structural Engineering*, 139(6), 1033-1042.

Vasdravellis G, Karavasilis TL, Uy B (2014). Design rules, experimental evaluation, and fracture models for high-strength and stainless steel hourglass shape energy dissipation devices. *Journal of Structural Engineering*, 140(11):04014087.

Vayas I, Thanopoulos P (2005). Innovative dissipative (INERD) pin connections for seismic resistant braced frames. *International Journal of Steel Structures*, 5(5):453-464.

Whittaker AS, Bertero VV, Thompson CL, Alonso LJ (1991). Seismic testing of steel plate energy dissipation devices. *Earthquake Spectra*, 7(4):563-604.